Strength of the Hubbard potential and its modification by breathing distortion in BaBiO$_3$

Alexander E. Lukyanov [ORCID],[1] Ivan A. Kovalev [ORCID],[1] Vyacheslav D. Neverov [ORCID],[1] Yaroslav V. Zhumagulov [ORCID],[2,1,*]
Andrey V. Krasavin [ORCID],[1] and Denis Kochan [ORCID][2]

[1]*National Research Nuclear University MEPhI, Kashirskoye shosse 31, Moscow 115409, Russian Federation*
[2]*Institute for Theoretical Physics, University of Regensburg, Regensburg 93040, Germany*

BaBiO$_3$ compound is known as an archetype example of a three-dimensional Holstein model with the realization of the charge-density wave state at half filling and the superconducting state when doped. Although many works are devoted to the study the electron–phonon interaction in BaBiO$_3$, the influence of the electron–electron Hubbard interaction on the electronic structure in this system is still under investigation. In our work, we obtain analytical expression for the screened Coulomb potential, and along with the basis of *ab initio*-computed maximally localized Wannier orbitals, we quantitatively estimate the magnitude of the effective on-site Hubbard potential scrutinizing the effects of distortion of the crystal lattice. We show that a proper inclusion of the electron–electron interactions into the Holstein model significantly lowers the value of the underlying electron–phonon coupling. Finally, we find that the amplitudes of the repulsive electron–electron potential and its attractive counterpart mediated by the electron–phonon coupling are rather comparable. This may open a way for a realization of the intermediate phase of BaBiO$_3$ in terms of the Holstein-Hubbard model.

I. INTRODUCTION

Perovskite compounds are of particular interest because of a large variety of physical phenomena they exhibit. A high degree of chemical functionalization and structural flexibility in combination with an inhomogeneous distribution of partially filled d states lead to a coexistence of several interactions that operate on spin, charge, lattice, and orbital degrees of freedom. Their mutual interplay generates a wide range of physical properties and functional capabilities counting colossal magnetoresistance [1,2], ferroelectricity [3], superconductivity in cuprates [4] and bismuthates [5,6], metal–insulator transition [7], ferromagnetism [8], topological insulators [9], etc.

Properties of many ABX$_3$-type perovskites—where A is a large cation, usually an alkaline earth or rare earth element, B is relatively small ion of 3d-, 4d-, or 5d-transition metal, and X are anions, usually oxygen atoms that form the octahedral environment of the B ion; see Fig. 1(a)—are extremely sensitive to distortion, rotation, and tilting of the BX$_6$ octahedra. These structural modifications and distortions control hopping amplitudes and exchange interactions through the lengths and angles of the octahedral B–X–B bonds and consequently, the underlying electronic and magnetic properties of the perovskites compounds [10,11].

BaBiO$_3$ is a remarkable representative of the perovskite class as it realizes high-temperature superconductivity while it does not include transition metal ions [6]. In normal conditions, BaBiO$_3$ is characterized by anomalously high amplitude of phonon oscillations leading to pronounced breathing and tilting distortions of the crystal structure [12]. The breathing distortion is caused by a tunneling of electron pairs and subsequent charge transfer between the neighboring octahedra; as a consequence, Bi-O bonds change their lengths and the octahedral pattern dynamically alters its proportions along three crystallographic directions [5,13,14]. Recently, it was established that the distortion amplitude in BaBiO$_3$ may be controlled by a strong laser pulse, which drives the system from insulating to metallic state with no distortions [15].

From a theoretical point of view, BaBiO$_3$ serves as an archetypal lattice model [6,16,17] for studying electron–phonon phenomena in perovskites as its electronic properties are defined mostly by a single effective orbital—the molecular Bi-O hybrid. The majority of recent works aimed to focus on the Holstein-like models [15,18–20], though some early reports found also a negative Hubbard-*U* parameter by employing first-principles calculations [21] or phenomenological considerations [22]. The use of the Holstein-like models in the above-mentioned studies put forward suggestions that the electron–phonon coupling dominates other interactions in BaBiO$_3$. Also, in a recent work [23] it was shown that by taking into account the screened Coulomb potential at the level of *GW* approximation [24] it can significantly increase the electron–phonon coupling in BaBiO$_3$. The central aim of this work is to demonstrate that the Coulomb interaction in BaBiO$_3$ is of considerable strength and affects the main electronic properties of the compound including the electron–phonon coupling itself, so the Coulomb repulsion should not be neglected. Also, we propose a certain modification of the Coulomb interaction on the model level taking into account an influence of the large distortions of the crystal lattice of BaBiO$_3$ with the electrons' pair tunneling among the neighboring octahedra.

For this purpose, we calculate electronic band structure, perform wannierization, and compute matrix elements of

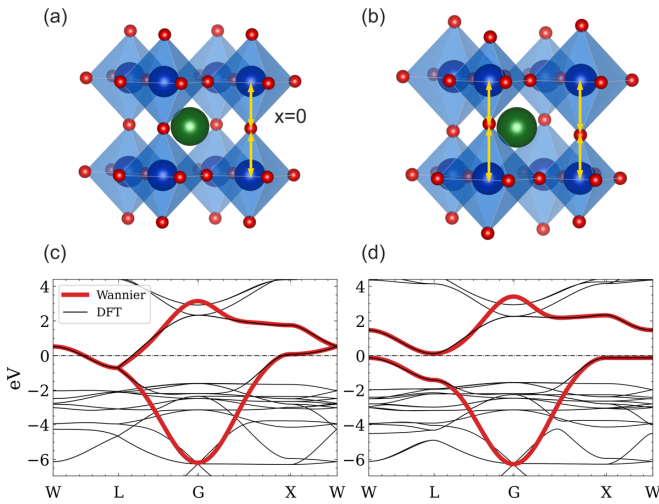*iaroslav.zhumagulov@physik.uni-regensburg.de

FIG. 1. The breathing distortion in $BaBiO_3$ and its effect on the electronic band structure. Bi ions are displayed in blue, O in red, and Ba in green. Panels (a) and (b) show schematically undistorted and distorted lattice structures with large and small octahedra parameterized by the length of Bi-O bond; yellow arrows indicate changes in their lengths and x stands for the corresponding distortion amplitude. Large octahedra host an additional pair of electrons, while the small ones have a pair of holes; the sizes of octahedra are exaggerated for clarity. Panels (c) and (d) show, correspondingly, the electronic band structures of undistorted and distorted $x = 0.1$ Å lattices; black lines correspond to *ab initio* calculations, while the red lines come from the effective tight-binding model (wannierization) that covers two bands near the Fermi level. A direct gap exists for any nonzero distortion, while the indirect one opens for the distortions above 0.1 Å.

the Coulomb interaction in the basis of *ab initio*-computed maximally localized Wannier orbitals—all that for different distortion amplitudes. Based on these calculations we estimate strengths of the underlying Holstein g and Hubbard U parameters that enter the effective lattice model. In this work, we restrict ourselves to the breathing mode displayed in Fig. 1, since the tilting distortions do not change significantly the electronic properties of $BaBiO_3$ [25].

The main difficulty associated with calculating the Coulomb matrix elements is of a technical nature: The calculation of the screened Coulomb potential requires exact convergence in many parameters, such as **k** mesh and the number of conduction bands [26–33]. To overcome this obstacle, we use a model of the dielectric function for calculating the screened Coulomb potential. Model dielectric functions were used to describe many-body effects in three-dimensional semiconductors long before the development of computer modeling of materials [34–37]; in recent years, this approach has gained relevance in the study of low-dimensional materials, in particular graphene [38], graphane [39], two-dimensional heterostructures [40], monolayers of transition metal dichalcogenides [41], etc. In this work we use the model dielectric function introduced by Cappellini *et al.* [37] and generalize it to account for nonlocal effects. It turns out that the integral for the screened Coulomb potential can be calculated analytically in the three-dimensional isotropic case

after which calculation of the Hubbard U becomes a relatively simple task.

The paper is organized as follows: Section II provides a theoretical basis for the methods employed in the sequel of the work; Section III presents details of the calculations and as well discusses the obtained results; finally, Section IV summarizes the work and outlines some perspectives.

II. MODEL

A. Model formulation—rationals

$BaBiO_3$ compound is used widely [19,22,42,43] as a textbook example of the Holstein model with the Hamiltonian

$$H_H = H_{el} + H_{ph} + H_{el-ph} \qquad (1)$$

that takes into account electronic and phononic degrees of freedom and also a strong electron–phonon interaction coupling them. The effective model Hamiltonian H_H operates on the single-orbital cubic lattice (at half filling) formed by Bi sites, since therein-centered Wannier orbitals dominate the $BaBiO_3$ band structure around the Fermi level; see the bold red bands mainly along the W-L and X-W paths in Figs. 1(c) and 1(d). Particular terms of H_H have the following structures (from now on we omit the Planck constant $\hbar$):

$$H_{el} = -\sum_{ij\sigma} t_{ij}(c_{j\sigma}^\dagger c_{i\sigma} + c_{i\sigma}^\dagger c_{j\sigma}), \qquad (2)$$

$$H_{ph} = \omega_{ph} \sum_i b_i^\dagger b_i, \qquad (3)$$

$$H_{el-ph} = g \sum_{i\sigma} (b_i^\dagger + b_i) n_{i\sigma}. \qquad (4)$$

Here $c_{i\sigma}^{(\dagger)}$ are the electron operators annihilating (creating) an electron with spin σ at site i, t_{ij} are the underlying hopping integrals, and $n_{i\sigma} = c_{i\sigma}^\dagger c_{i\sigma}$ are the corresponding number operators. Moreover, we consider a single phonon mode with frequency ω_{ph}, which makes the main contribution to the electronic properties of the compound [25,44] and ascribe it at each lattice site i phononic annihilation (creation) operators $b_i^{(\dagger)}$. This mode represents the optical breathing distortion in $BaBiO_3$. Down-to-earth, oxygen octahedra around the Bi sites "breath," i.e., they compress and expand in time varying their volumes around some average (site independent) value V_0. Denoting for each Bi site i the corresponding instantaneous octahedral volume as V_i, one can define for each i the scalar quantity $x_i = \sqrt[3]{V_i - V_0}$, which can in turn be expressed as a linear combination of the above defined on-site bosonic operators, i.e., $x_i \sim b_i^\dagger + b_i$. We ascribe to the latter kinetic energy, Eq. (3), and couple them with the electron density, see Eq. (4), via the Holstein-like on-site electron–phonon coupling g. Its explicit value in terms of DFT data is given below along with other interaction constants. Although it is widely accepted that the Holstein model describes systems sufficiently well, in our work we would like to go beyond it and consider additional interactions to the Holstein Hamiltonian H_H, Eq. (1). Particularly, we study the *on-site Hubbard* interaction H_U and its associate *on-site Hubbard–phonon* interaction H_{U-ph} triggered by the action of the optical breathing phonon mode:

$$H_U = U \sum_i n_{i\uparrow} n_{i\downarrow}, \qquad (5)$$

$$H_{U-\text{ph}} = \gamma \sum_i (b_i^\dagger + b_i) n_{i\uparrow} n_{i\downarrow}. \tag{6}$$

Consequently, we term U as the on-site Hubbard coupling and γ as the on-site Hubbard–phonon coupling. Although the role of the Hubbard term is clear, it is worth saying why we care to introduce the Hubbard–phonon term. The breathing distortion in BaBiO$_3$ is accompanied by a tunneling of the electron/hole pairs and hence a substantial charge transfer between the neighboring Bi-centered octahedra. For that reason we expect in our "poor-man extension" of the Holstein–Hubbard model also a certain coupling between the phonons and the pair-density operator, i.e., $n_{i\uparrow} n_{i\downarrow}$-term (a sort of "back-(re)action" the electron-pairs leave on phonon subsystem). However, integrating out phonon degrees of freedom, we can down-fold $H_{U-\text{ph}}$ and $H_{\text{el}-\text{ph}}$ Hamiltonians into effective on-site electron–electron interactions of the Hubbard-type but with dynamical dependence on ω:

$$H_{U-\text{ph}}(\omega) = \gamma^2 \frac{2\omega_{\text{ph}}}{\omega^2 - \omega_{\text{ph}}^2} \sum_i n_{i\uparrow} n_{i\downarrow}, \tag{7}$$

$$H_{\text{el}-\text{ph}}(\omega) = g^2 \frac{2\omega_{\text{ph}}}{\omega^2 - \omega_{\text{ph}}^2} \sum_i n_{i\uparrow} n_{i\downarrow}. \tag{8}$$

It is clear from the above expressions that bringing back phonon degrees of freedom their sum would behave as a sole electron–phonon interaction with the renormalized electron–phonon coupling strength:

$$g^* = \sqrt{g^2 + \gamma^2}. \tag{9}$$

Thus, we can conclude that the fluctuations of the on-site Hubbard potential U enhance the electron–phonon coupling constant g. It is obvious that the presence of electron–electron interactions has a significant impact on the underlying electronic structure of the system and its phase diagram—it is known that the Holstein–Hubbard model, $H_H + H_U$—leads to a different phase diagram as that predicted by its less-interactive Holstein ancestor [45–57]. In this regard, the electron–electron repulsive interaction can contra act the attractive interaction mediated by electron–phonon coupling, lowering its strength and possibly even turning the attraction into an effective repulsion. The aim of our work is to estimate magnitudes of t_{ij}, g, U, and γ using *ab initio* calculations and analytical results about screening.

B. Estimation of the model parameters: Conceptuals

The starting point is the *ab initio* calculation of the electronic band structure of BaBiO$_3$ subjected to different distortion amplitudes of the frozen breathing mode; see Fig. 1 for the structure visualization and its electronic band structure. We have calculated electronic band structures for several representative breathing distortions starting from the undistorted system; for more details, see Section III.

Since we aim to capture physics around the Fermi level we focus on two closest bands in its vicinity—the central bands evolving mainly along the W-L and X-W paths in Figs. 1(c) and 1(d) spanning roughly the energy window from −2 to
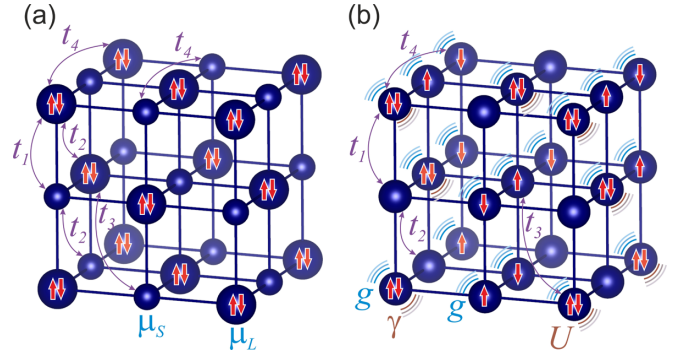

FIG. 2. Schematic mapping of the single-orbital tight-binding Hamiltonian onto the interacting Holstein–Hubbard model. (a) The effective single-orbital tight-binding model Hamiltonian is defined on a cubic lattice with the nonequivalent s and L nearest-neighbor Bi sites with different on-site energies μ_s and μ_L. The hopping integrals t_i are taken into account up to the fourth coordination number. In reality this picture dynamically evolves in time and hence s and L octahedra occupy different lattice sites. To visualize a fact that the large octahedra host extra electron pairs, the L sites (with on-site energy μ_L) are displayed as pair occupied. (b) The interacting Holstein–Hubbard model is defined on a cubic lattice with equivalent sites but varying electron occupancies. Singly occupied sites give rise to the Holstein electron–phonon interaction with the coupling strength g, while the doubly occupied sites interact also via the Hubbard and the Hubbard–phonon interactions parameterized by U and γ. Kinetic part of the Holstein–Hubbard model involving single-electron hoppings t_i is the same as in panel (a), phonons are displayed as concentric blue-brown wave echos around Bi sites.

2 eV. These two bands are further subjected to the wannerization procedure that gives us an effective single-orbital tight-binding model Hamiltonian H_{TB} acting on the cubic lattice with two nonequivalent nearest-neighbor Bi sites; see Fig. 2. This is quite reasonable since the two neighboring Bi atoms within BaBiO$_3$ are surrounded by two spatially different octahedra and hence different charge environments. We call the Bi sites surrounded by the small (compressed) and large (expanded) octahedra the small and large sites, reserving for them the subscripts "s" and "L;" correspondingly, when necessary, we talk also about the "s" and "L" sublattices of the cubic crystal. The effective tight-binding Hamiltonian H_{TB} stemming from the wannierization is parameterized by the hopping integrals t_{ij} and the on-site energies μ_s and μ_L,

$$H_{\text{TB}} = -\sum_{ij\sigma} t_{ij}(c_{j\sigma}^\dagger c_{i\sigma} + c_{i\sigma}^\dagger c_{j\sigma})$$
$$+ \mu_s \sum_{i\in s,\sigma} c_{i\sigma}^\dagger c_{i\sigma} + \mu_L \sum_{i\in L,\sigma} c_{i\sigma}^\dagger c_{i\sigma}, \tag{10}$$

whose values are summarized in Table I for different distortion strengths x. The sum in the first (kinetic) term of H_{TB} runs over the first up to the fourth-nearest neighbors, and the corresponding hopping integrals among them are denoted as $t_1, \ldots, t_4$ in Table I. As a comment, due to the nonequivalent "s" and "L" sites, the cubic unit cell of the tight-binding model is twice as large as the corresponding cubic unit cell of the

TABLE I. Effective model parameters for BaBiO$_3$ compound subjected to various amplitudes of the breathing distortion parameterized by x. Tight-binding model stemming from the wannierization, Eq. (10), involves the on-site energies μ_s and μ_L at two nonequivalent Bi sites and the hoppings integrals t_i, $i = 1, ..., 4$, ranging among the corresponding ith nearest neighbors within the underlying cubic lattice; for a schematic, see Fig. 2. On-site energies μ's scale linearly with x, while t_i's are only mildly fluctuating at second decimal place. To keep the table concise we only show data for a limited set of x; the values for remaining μ's can be easily interpolated.

x [Å]	μ_s [eV]	μ_L [eV]	t_1 [eV]	t_2 [eV]	t_3 [eV]	t_4 [eV]
0.000	−0.088	−0.088	−0.514	−0.130	−0.056	0.078
0.100	0.758	−0.808	−0.542	−0.151	−0.049	0.085
0.125	0.972	−1.000	−0.539	−0.170	−0.063	0.083
0.150	1.199	−1.125	−0.532	−0.177	−0.061	0.088
0.175	1.401	−1.256	−0.524	−0.187	−0.062	0.097

Holstein model. For the latter the breaking of the sublattice symmetry appears dynamically as a result of the electron–phonon coupling with the breathing optical phonon mode.

Since the hoppings integrals entering H_{TB}, Eq. (10), are relatively weakly dependent on the distortion x, we can naturally identify the kinetic part of the Holstein model, Hamiltonian H_{el}, Eq. (2), with the kinetic part of the wannierization-generated tight-binding model, i.e.,

$$H_{el} = \text{kinetic term of } H_{TB}. \quad (11)$$

Contrary, the on-site energies μ_s and μ_L are very strongly distortion dependent, meaning the electron–phonon coupling with the breathing mode in BaBiO$_3$ is sufficient. On the level of the Holstein model such coupling is governed by the Hamiltonian H_{el-ph}, Eq. (4), where the coupling constant g can be estimated as follows:

$$g = \frac{\partial \mu}{\partial x} \sqrt{\frac{1}{2M_O \omega_{ph}}}, \quad (12)$$

where $\mu = (\mu_s - \mu_L)/2$ is the (interpolated) difference (function) of two on-site energies entering H_{TB}, M_O is the oxygen mass, $\omega_{ph} = 70$ meV [58,59] is the optical phonon energy and x is the amplitude of the breathing distortion.

The second outcome of the wannierization are maximally localized Wannier orbitals $w_{i,s}$ and $w_{i,L}$ centered on different "s" and "L" lattice sites. In what follows we pick up two neighboring sites and use the centered Wannier orbitals—we denote them as w_s and w_L—for the calculation of the Hubbard and Hubbard–phonon coupling strengths. For the iso-surface visualization of w_s and w_L for the undistorted and distorted lattice, see Figs. 4(a) and 4(b).

Calculating the matrix elements of the Coulomb interaction in terms of the tight-binding model based on the *ab initio*

calculation is a computationally complex problem, since it requires calculation of the screened Coulomb potential by the random-phase approximation method [24,26,28,36]. To get rid of this problem, we use the model dielectric function from Ref. [37],

$$\epsilon(\mathbf{q}, \mathbf{r}) = 1 + \left[\frac{1}{\epsilon_\infty - 1} + \alpha \frac{q^2}{q_{TF}^2(\mathbf{r})} + \frac{q^4}{4m^2\omega_p^2(\mathbf{r})} \right]^{-1}, \quad (13)$$

where ϵ_∞ is the long-wave length ($q = 0$) limit of the dielectric constant specific for each material, and $q_{TF}(\mathbf{r})$ and $\omega_p(\mathbf{r})$ are, correspondingly, the Thomas–Fermi wave vector and the plasma frequency that are explicit functions of the valence electron density $\rho(\mathbf{r})$, $q_{TF}^2 = 4(3\rho(\mathbf{r})/\pi)^{1/3}$, $\omega_p^2 = 4\pi\rho(\mathbf{r})$. The only dimensionless fitting parameter α was obtained in Ref. [37] by employing *ab initio* calculations. Moreover, it turned out that α is practically independent on the choice of material. In our work, we therefore use a rather universal value of $\alpha = 1.563$ originally estimated in Ref. [37]. The above choice of the dielectric function is because of its relative simplicity, analytical possibility of deriving the screened potential explicitly, and physically appropriate description of the screening on both long and short ranges.

The matrix elements of the screened Coulomb interaction between two Wannier orbitals w_n and w_m (n, m run through {s, L}) are expressed as

$$W_{nm} = \frac{1}{2} \int d\mathbf{r}d\mathbf{r}' |w_n(\mathbf{r})|^2 W(\mathbf{r} - \mathbf{r}', \rho(\mathbf{r}))|w_m(\mathbf{r}')|^2$$
$$+ \frac{1}{2} \int d\mathbf{r}d\mathbf{r}' |w_n(\mathbf{r})|^2 W(\mathbf{r} - \mathbf{r}', \rho(\mathbf{r}'))|w_m(\mathbf{r}')|^2, \quad (14)$$

where $W = \epsilon^{-1} V$ is the screened Coulomb potential by means of the above dielectric function. Within this approach, the matrix elements W_{nm} can be calculated without significant computational costs. This is because the difference between the screened, W, and the bare V Coulomb interaction, the so-called *correlated Coulomb potential*, $W_c = W - V$, can be represented in the explicitly analytical form. Performing Fourier transformation of W_c [24],

$$W_c(\mathbf{r}) = \frac{1}{(2\pi)^3} \int d^3\mathbf{q} \frac{4\pi e^2}{q^2} \left[\frac{1}{\epsilon(\mathbf{q}, \rho(\mathbf{r}))} - 1 \right] e^{i\mathbf{q}\mathbf{r}}, \quad (15)$$

one arrives in the case of spherical symmetry at the final expression that counts just material parameters and the magnitude of spatial distance $r = |\mathbf{r}|$:

$$W_c(r) = -\frac{e^2}{2r} \left(1 - \frac{1}{\epsilon_\infty} \right) \text{Re} \left\{ 2 - \frac{1+A}{A} e^{-\kappa r\sqrt{1-A}} \right.$$
$$\left. + \frac{1-A}{A} e^{-\kappa r\sqrt{1+A}} \right\}, \quad (16)$$

or

$$W_c(r) = \begin{cases} -\frac{e^2}{2r}\left(1 - \frac{1}{\epsilon_\infty}\right)\left[2 - \frac{1+A}{A}e^{-\kappa r\sqrt{1-A}} + \frac{1-A}{A}e^{-\kappa r\sqrt{1+A}}\right]; & \zeta < 1, \\ -\frac{e^2}{r}\left(1 - \frac{1}{\epsilon_\infty}\right)\left[1 - e^{-\kappa ra}\left(\cos\kappa rb + \frac{1}{A}\sin\kappa rb\right)\right]; & \zeta > 1, \ a = \sqrt{\frac{\sqrt{\zeta}+1}{2}}, \ b = \sqrt{\frac{\sqrt{\zeta}-1}{2}} \end{cases} \quad (17)$$

with

$$A = \sqrt{|1 - \zeta|}, \quad \kappa = \frac{(2\alpha)^{1/2}\pi^{2/3}}{3^{1/6}}\rho(\mathbf{r})^{1/3}. \quad (18)$$

Here ζ is the dimensionless parameter,

$$\zeta = \frac{\xi}{a_0\rho(\mathbf{r})^{1/3}}, \quad (19)$$

where a_0 is the Bohr radius and

$$\xi = \frac{4 \cdot 3^{2/3}}{\pi^{5/3}\alpha^2}\frac{\epsilon_\infty}{\epsilon_\infty - 1}. \quad (20)$$

The detailed derivation of Eq. (17) is presented in the Appendix.

The matrix elements W_{nm} are then obtained as the sum of the matrix elements of the correlated Coulomb potential, $W_{c,nm}$, and those of the bare Coulomb interaction,

$$V_{nm} = \int d\mathbf{r} d\mathbf{r}' |w_n(\mathbf{r})|^2 V(\mathbf{r} - \mathbf{r}')|w_m(\mathbf{r}')|^2. \quad (21)$$

As a comment, W_{nm} depends on the distortion x, since the latter affects "shapes" of the Wannier orbitals w_n and w_m, see Fig. 4, and also the charge distribution $\rho(\mathbf{r})$ entering the dielectric function ϵ, Eq. (13).

In the next step, the self-screening issues should be properly taken into account. An electron cannot screen itself, which makes calculations using the random phase approximation inappropriate. Therefore, it is conceptually erroneous to estimate the Hubbard U parameter in terms of the fully screened Coulomb potential W. To avoid the double screening, one usually uses the constrained random-phase approximation (cRPA) [26], which is a sort of the unscreening procedure that takes fully screened Coulomb matrix elements W_{nm} and provides their partly unscreened-representatives, W_{nm}^r, facilitated for the bands defined by the effective tight-binding model. Within cRPA, the matrix elements of the Coulomb interaction, W_{nm}^r, can be expressed in the following way [26–28,32,60]:

$$W^r = W[I + P^d W]^{-1}, \quad (22)$$

where W represents the fully screened Coulomb interaction, Eq. (14), and P^d is the band subspace polarization specified by entries of the effective tight-binding model. Down to earth, the band subspace polarization can be calculated as [24,26,33,35]

$$P_{nm}^d = \frac{g_s}{N_k^2}\sum_{\mathbf{kq},\alpha\beta}\frac{f_\beta(\mathbf{k}) - f_\alpha(\mathbf{k} + \mathbf{q})}{E_\beta(\mathbf{k}) - E_\alpha(\mathbf{k} + \mathbf{q})}$$
$$\times C_{n,\beta}(\mathbf{k})C_{n,\alpha}^*(\mathbf{k} + \mathbf{q})C_{m,\beta}^*(\mathbf{k})C_{m,\alpha}(\mathbf{k} + \mathbf{q}), \quad (23)$$

where $g_s = 2$ is the spin degeneracy factor, N_k is the number of $\mathbf{k}$ points in the Brillouin zone, $n, m \in \{s, L\}$, sum over α and β runs over the valence and conduction bands of the underlying tight-binding model, $E_\alpha(\mathbf{k})$ is the tight-binding single-particle energy, $f_\alpha(\mathbf{k})$ is the corresponding Fermi–Dirac occupation, and $C_{n,\alpha}(\mathbf{k})$ is the probability amplitude giving contribution of the nth Wannier orbital to the αth Bloch-band state with momentum $\mathbf{k}$. Finally, equipped with the partly screened Coulomb matrix elements W_{nm}^r, we calculate [32,60] the optimal values of the on-site Hubbard U

parameter and the Hubbard–phonon coupling γ:

$$U_s = W_{ss}^r - W_{sL}^r, \quad U_L = W_{LL}^r - W_{sL}^r, \quad (24)$$

$$U = \frac{1}{2}\langle U_s + U_L\rangle_x, \quad (25)$$

$$\gamma = \frac{\partial U}{\partial x}\sqrt{\frac{1}{2M_O\omega_{ph}}}. \quad (26)$$

As a comment, $U_{s/L}$ and U are understood as the interpolated functions of the distortion x that is entering W_{nm}^r and from them derived quantities. Symbol $\langle A\rangle_x$ represents an average value of the quantity A taken over the range of crystal lattice distortions.

In this work, we consider a single-orbital tight-binding model since it fully incorporates physics of the BaBiO$_3$ near the Fermi energy level. However, all of the above equations and concepts can be naturally extended to involve multiorbital models.

III. RESULTS AND COMPUTATIONAL DETAILS

The basis for estimating the model parameters entering the Holstein, Eq. (1), and the Hubbard Hamiltonian, Eq. (5), is built on the Wannier orbitals that were obtained from the *ab initio* calculations using numerical packages *Quantum Espresso* [61] and *Wannier90* [62]. For bismuth, barium, and oxygen atoms, the norm-conserving semirelativistic LDA pseudopotentials from the Pseudo Dojo database [63] were used and the energy cutoff for the plane-wave basis was set at 120 Ry with convergence accuracy of 10^{-8}. Frozen lattice distortion due to the breathing mode leads to the doubling ("s" and "L" sites) of the unit cell along the (111) direction owing to the underlying crystal the cubic face-centered lattice. We have performed several calculations for representative values of the breathing distortion x starting from the undistorted metallic system and continuing by varying x in steps of 0.025 Å. For distortions below 0.1 Å the system is metallic; see Figs. 1(c) and 1(d), and possesses a nonzero direct gap; however, going above 0.1 Å it turns into an indirect insulator—for the evolution of the direct and indirect gaps with the distortion; see Fig. 3(a). Our findings are in good agreement with the known experimental result [12] affirming the BaBiO$_3$ compound to be the indirect-gap insulator for $x = 0.1$ Å.

To proceed further, the two bands in the vicinity of the Fermi level, see Figs. 1(c) and 1(d), were subjected to the wannerization procedure that provided us an effective single-orbital (per Bi atom) tight-binding Hamiltonian H_{TB}, Eq. (10), reliable in the energy window from -2 to 2 eV. The obtained electron hopping integrals $t_1, \ldots, t_4$, Table I, and the derived value of the electron–phonon coupling constant, Eq. (12),

$$g = 0.32 \pm 0.01 \text{ [eV]}, \quad (27)$$

agree well with the known results [25]. Wannierization yielded us also Wannier orbitals w_s and w_L, whose iso-surface plots are displayed for the undistorted and distorted cases in Fig. 4. As it is seen, the Wannier orbitals are centered on the Bi atoms and form molecular-hybrids counting s orbital from the bismuth and p orbitals from the surrounding oxygens
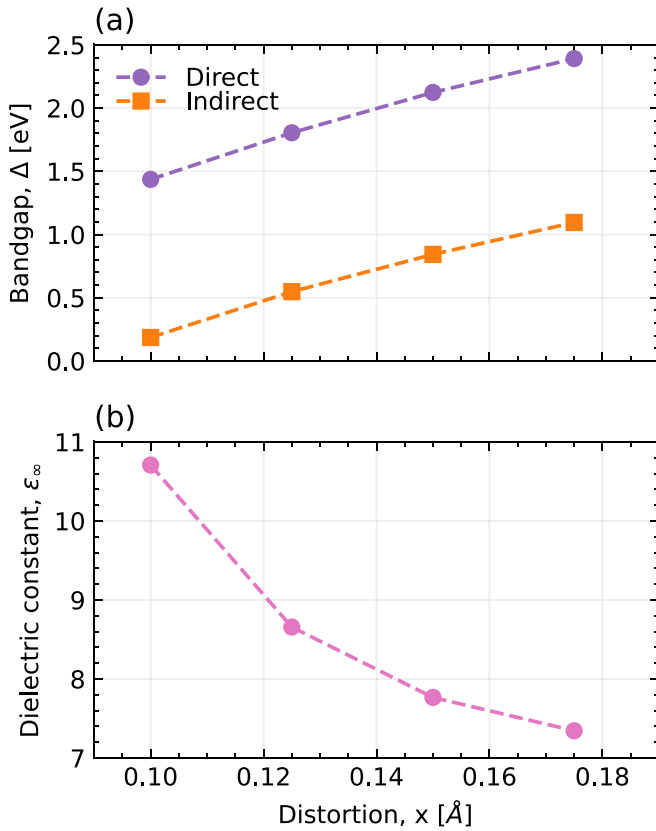
FIG. 3. Dependence of the direct and indirect band gaps, panel (a), and long-range dielectric constant ϵ_∞, panel (b), on the BaBiO$_3$ breathing distortion amplitude x. The direct gap (circles) opens gradually with the appearance of the distortion, while the indirect gap (squares) is absent and emerges only for x above 0.1 Å. Correspondingly, in the metallic state the system has an infinite dielectric constant ϵ_∞, which is then descending toward finite values—the larger the indirect gap the more the insulating system behaves and hence the smaller is ϵ_∞.

(directed toward the Bi atoms). The spreads, Ω, of the Wannier orbitals, defined as the expectation value $\Omega = \langle \mathbf{r}^2 \rangle - \langle \mathbf{r} \rangle^2$, were calculated using the procedure described in Ref. [64]. The spreads for two nonequivalent Wannier orbitals w_s and w_L increase with the increased lattice distortion, but not identically. As it is clear from Fig. 5, the spread of w_L increases more significantly than that of w_s, what affects a scaling of the underlying Coulomb interaction with x.

Our goal is the calculation the Hubbard parameters U_s and U_L, for which we need apart of the Wannier states discussed above also the long-range dielectric constant ϵ_∞; see Eqs. (13) and (17). The values of ϵ_∞ for the gapped systems, i.e., for $x > 0.1$ Å, are obtained by the DFPT method built in the numerical package *Quantum Espresso* [61]. The results are shown in Fig. 3; with an increased amplitude of the lattice distortion, the value of ϵ_∞ decreases (pink dot symbols) while the size of the indirect gap rises (orange square symbols); obviously, as the system becomes more insulating, the dielectric screening softens. In the metallic state, $x < 0.1$ Å, the dielectric screening is strong (infinite).

Equipped with the dielectric constant ϵ_∞ and the Wannier orbitals w_s and w_L we are ready to calculate the bare and
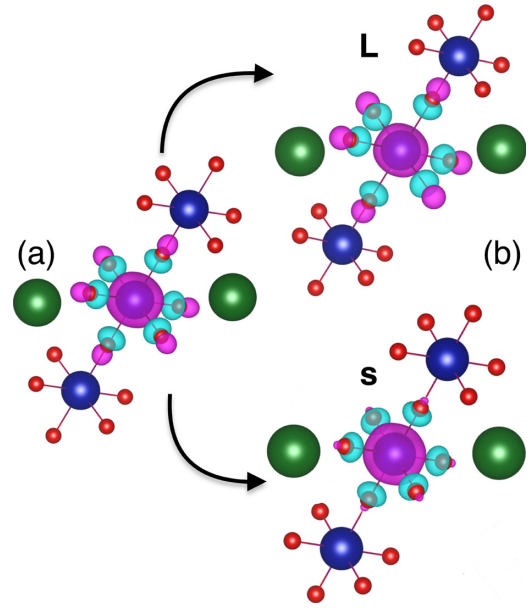

FIG. 4. Iso surfaces of the underlying Wannier orbitals w_s and w_L. Panels (a) and (b) show, correspondingly, the iso surfaces of the undistorted, $x = 0$, and distorted, $x = 0.175$ Å, Wannier orbitals. In panel (a) both iso surfaces coincide, while in panel (b) the upper iso surface corresponds to w_L and the lower for w_s; all iso surfaces are displayed for the same iso level. Positive and negative values are shown in light blue and pink, respectively; the colors of atoms are the same as in Fig. 1.

screened Coulomb matrix elements V_{nm} and W_{nm}^r that are needed for further estimation of the Hubbard parameters U_s and U_L. Increased spread of the Wannier orbitals, Fig. 5, lowers the magnitudes of the Hubbard parameters and also counterbalances the screening in the system by decreasing the dielectric constant. Summing up these two effects, we obtain a slightly nonlinear dependence of the Hubbard parameters on the amplitude of the crystal lattice distortion, Fig. 6(a). However, the difference between local Hubbard parameters $U_s - U_L$ is strictly linear, Fig. 6(b), which is consistent with the above Hamiltonian $H_{U-\mathrm{ph}}$ Eq. (6).
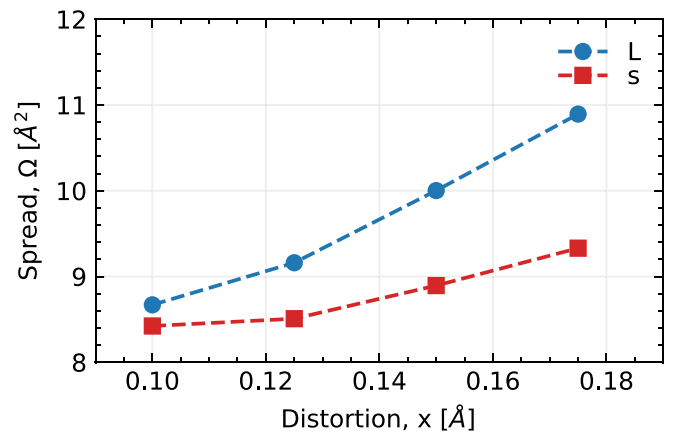

FIG. 5. Spreadings, $\Omega = \langle \mathbf{r}^2 \rangle - \langle \mathbf{r} \rangle^2$, of the Wannier functions depending on the distortion. Red and blue colors correspond to w_s and w_L Wannier states; dashed lines are guides to the eye.
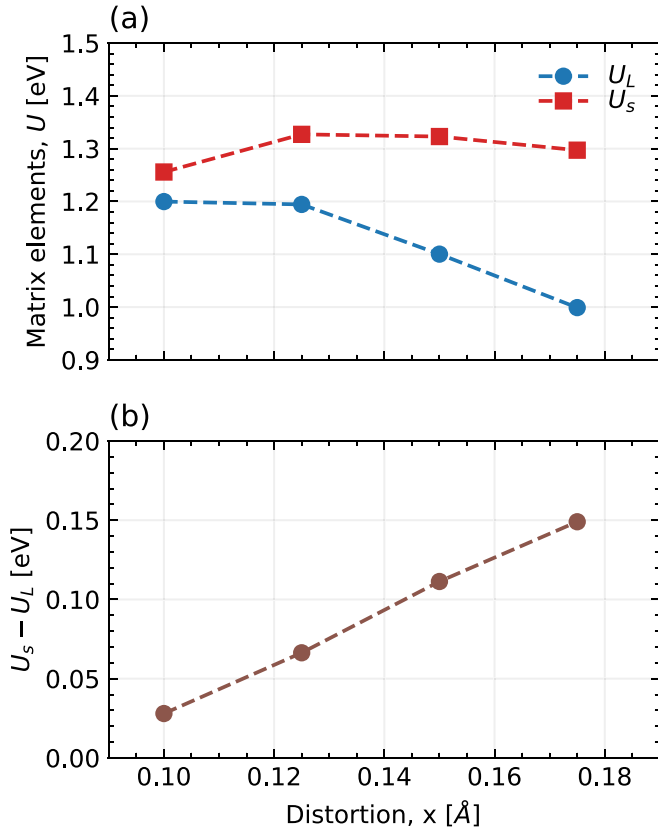
FIG. 6. Evolution of the Hubbard parameters U_s and U_L, panel (a), and their difference $U_s - U_L$, panel (b), with distortion.

The values of the on-site Hubbard potential U and the on-site Hubbard–phonon coupling γ that are naturally emerging from the nonlocal screening and the coupling to the breathing phonon mode can be estimated based on Eqs. (25) and (26). Using obtained values of $W^r_{nm}(x)$ and the reference energy of the breathing Raman mode, $\omega_{ph} = 70$ meV [58,59], the resulting values read

$$U = \left\langle \tfrac{1}{2}\left[W^r_{ss} + W^r_{LL}\right] - W^r_{sL}\right\rangle_x = 1.21 \pm 0.12 \,[\text{eV}]; \quad (28)$$

$$\gamma = (1.63 \pm 0.04)\,[\text{eV/Å}] \times 0.043\,[\text{Å}]$$
$$= 0.070 \pm 0.002\,[\text{eV}]. \quad (29)$$

To estimate the error, we used the three sigma rule. Thus we can calculate the correction to the electron–phonon coupling constant as

$$g^* = \sqrt{g^2 + \gamma^2} = 0.33 \pm 0.01\,[\text{eV}]. \quad (30)$$

It is well known that the Hubbard and Holstein interactions—parameterized by U and g couplings—act on an electronic system at the half filling in the opposite way. The Hubbard interaction tends to transfer the system into the Mott insulator regime with a uniform charge distribution, while the Holstein interaction strives to form a charge-density wave (CDW) with a spatially nonuniform charge rearrangement. In the effect, the repulsive Hubbard coupling triggered by the Coulomb interaction gets contra acted by an attractive electron–electron interaction resulting from the Holstein coupling of electrons and phonons. The final on-site potential—in the antiadiabatic

approximation—can be quantified by the following expression [45,57]:

$$U^* := U - \frac{2g^{*2}}{\omega_{ph}} = U - \lambda D =: -\lambda^* D, \quad (31)$$

where $\lambda = 2g^{*2}/(\omega_{ph}D)$ is the dimensionless strength of the Holstein + Hubbard–phonon attraction and D is the effective bandwidth, for our model $D = 4$ eV. The resulting on-site electron–electron interaction U^* can be repulsive or attractive giving rise to the Mott insulator or CDW physics. In the latter case, the right-hand side of Eq. (31) defines an effective dimensionless "electron–phonon strength" $\lambda^* = \lambda + \delta\lambda = \lambda - U/D < \lambda$, whose value gets reduced by $\delta\lambda = -U/D$. The final estimations give

$$U^* = U - \frac{2g^{*2}}{\omega_{ph}} = (1.21 - 3.06)\,[\text{eV}] = -1.85\,[\text{eV}] \quad (32)$$

$$\lambda^* = \lambda + \delta\lambda = 0.765 - 0.3025 = 0.4625. \quad (33)$$

So, we conclude that taking into account the Hubbard repulsion U, the effective on-site electron–electron interaction U^* is significantly suppressed as compared to the Holstein and Hubbard–phonon attractions $\lambda D = 2g^{*2}/(\omega_{ph})$. Without considering the Hubbard potential, we have $\lambda = 0.765$ and with $\lambda^* = 0.4625$. Comparing λ^* with λ we see that such suppression is about 40%. The frequency of the phonon mode $\omega_{ph} = 70$ meV is lower than the bandwidth $D = 4$ eV, which means that the antiadiabatic approximation is not fully valid. However, this sets the upper limit for estimating the magnitude of the electron–phonon interaction constant. Our conclusions partly contradict the recent results obtained by *GW* approximation [23], which gives $\lambda = 0.47$ before and $\lambda^* = 1.14$ after taking into account the screened Coulomb potential. A substantial difference is in the way the local Hubbard interaction is taken into account when calculating the effective constant of the electron–phonon interaction. At the same time, our findings are in agreement with the results of Ref. [23], since we also observe an increase in the electron–phonon coupling constant g^* due to fluctuations of the Hubbard potential.

These results show that by neglecting the Coulomb interaction, the value of λ would be overestimated and hence also the value of the band gap of $BaBiO_3$ realizing the CDW phase. Matrix elements of the Hubbard potential can show their significance for the description of physics of the electronic structure of $BaBiO_3$ and for the analyses of the phase transitions in the Holstein–Hubbard model [46,48–50,53,55,57] separating the antiferromagnetic ordering of the Mott insulator from that of the CDW phase. Perhaps the interplay of two interactions, an attractive electron–phonon and a repulsive electron–electron with strengths close in magnitude, may lead to the realization of the high-temperature superconductivity of the $BaBiO_3$ compound.

IV. CONCLUSIONS AND PERSPECTIVES

In our work, we estimated the magnitude of the on-site Hubbard potential in the $BaBiO_3$ using the analytical form of the screened Coulomb potential and the basis of the *ab initio*-computed maximally localized Wannier orbitals. Our results

show that the magnitude of the repulsive electron–electron Hubbard potential is comparable to the attractive potential of the electron–phonon + Hubbard–phonon interactions. Therefore, their effective dimensionless attractive constant λ^* gets lowered by 40%. This indicates a significant contribution of the electron–electron interaction to the electronic structure of BaBiO$_3$. Although this modification of the Hubbard potential is difficult to take into account in the framework of the standard Migdal–Eliashberg theory [65], we assume a possible implementation of quantum Monte Carlo methods [47,54] taking into account these corrections. The electron–phonon interaction and the electron–electron interaction have the same order of magnitude in our calculations, which indicates the possibility of the realization of an intermediate phase between the antiferromagnetic ordering of the Mott insulator and the band insulator phase of the CDW. This opens the way for further research in the field of the origin of the superconducting state in the BaBiO$_3$ compound.

ACKNOWLEDGMENTS

APPENDIX: DERIVATION OF W_c

Below we describe the main steps in evaluating the following integral:

$$W_c(\mathbf{r}) = \frac{1}{(2\pi)^3} \int d^3\mathbf{q} \frac{4\pi e^2}{q^2} \left[\frac{1}{\epsilon(\mathbf{q}, \rho(\mathbf{r}))} - 1 \right] e^{i\mathbf{q}\mathbf{r}}. \quad (A1)$$

Since the integral is spherically symmetric it can be expressed in the following way:

$$W_c(\mathbf{r}) = -\frac{1}{\gamma} \int d^3\mathbf{q} \frac{1}{q^2} \frac{1}{b + aq^2 + q^4} e^{i\mathbf{q}\mathbf{r}}$$
$$= -\frac{2\pi}{\gamma} \int_0^\infty q^2 \frac{dq}{q^2} \frac{1}{b + aq^2 + q^4} \int_0^\pi d\theta \sin\theta e^{iqr\cos\theta}$$

$$= -\frac{4\pi}{\gamma r} \int_0^\infty dq \frac{\sin(qr)}{q(b + aq^2 + q^4)} \equiv -\frac{4\pi}{\gamma r} I_0(r), \quad (A2)$$

where

$$\gamma = \frac{2}{4m^2\omega_p^2}, \quad b = \frac{1}{\gamma}\left(1 + \frac{1}{\epsilon_\infty - 1}\right), \quad a = \frac{1}{\gamma}\frac{\alpha}{q_{\text{TF}}^2}. \quad (A3)$$

Obviously, $I_0(r)$, as defined by Eq. (A2), is zero for $r = 0$. As the next step we differentiate $I_0(r)$ with respect to r taken as parameter and make use of the residue theorem by properly closing contours in the complex plane:

$$I_0'(r) \equiv \frac{d}{dr} I_0(r) = \int_{-\infty}^\infty dq \frac{\cos(qr)/2}{(b + aq^2 + q^4)}$$
$$= \text{Re}\left\{ 2\pi i \sum_{\text{res}} \frac{e^{iqr}/2}{(b + aq^2 + q^4)} \right\}$$
$$= \text{Re}\left\{ \frac{\pi}{2}\left(\frac{e^{-r\sqrt{\chi_1}}}{\sqrt{\chi_1}(\chi_2 - \chi_1)} - \frac{e^{-r\sqrt{\chi_2}}}{\sqrt{\chi_2}(\chi_2 - \chi_1)} \right) \right\}$$
$$(A4)$$

with

$$\chi_{1,2} = \frac{a \pm \sqrt{a^2 - 4b}}{2}, \quad (A5)$$

the complex branches of the square roots should be chosen in such a way that $\text{Re}[\chi_{1,2}] > 0$. Integrating Eq. (A4) with respect to r we arrive at

$$I_0(r) = \int_0^r I_0'(u)du$$
$$= \text{Re}\left\{ \frac{\pi}{2(\chi_2 - \chi_1)}\left(\frac{1 - e^{-r\sqrt{\chi_1}}}{\chi_1} - \frac{1 - e^{-r\sqrt{\chi_2}}}{\chi_2} \right) \right\}.$$
$$(A6)$$

After backward substitutions we obtain

$$W_c(r) = -\frac{e^2}{2r}\left(1 - \frac{1}{\epsilon_\infty}\right)\text{Re}\left\{ 2 - \frac{A_+}{A}e^{-\kappa r\sqrt{A_-}} + \frac{A_-}{A}e^{-\kappa r\sqrt{A_+}} \right\},$$
$$(A7)$$

where

$$A = \sqrt{1 - \frac{2q_{\text{TF}}^2}{\alpha\kappa^2}\frac{\epsilon_\infty}{\epsilon_\infty - 1}}; \quad (A8)$$

$$\kappa = \frac{(2\alpha)^{1/2}\pi^{2/3}}{3^{1/6}}\rho(\mathbf{r})^{1/3}; \quad A_\pm = 1 \pm A. \quad (A9)$$

[1] M. B. Salamon and M. Jaime, The physics of manganites: Structure and transport, Rev. Mod. Phys. **73**, 583 (2001).

[2] R. von Helmolt, J. Wecker, B. Holzapfel, L. Schultz, and K. Samwer, Giant Negative Magnetoresistance in Perovskitelike La$_{2/3}$Ba$_{1/3}$MnO$_x$ ferromagnetic films, Phys. Rev. Lett. **71**, 2331 (1993).

[3] R. E. Cohen, Origin of ferroelectricity in perovskite oxides, Nature (London) **358**, 136 (1992).

[4] J. G. Bednorz and K. A. Müller, Possible high T$_c$ superconductivity in the Ba-La-Cu-O system, Z. Phys. B **64**, 189 (1986).

[5] A. Sleight, J. Gillson, and P. Bierstedt, High-temperature superconductivity in the BaPb$_{1-x}$Bi$_x$O$_3$ systems, Solid State Commun. **17**, 27 (1975).

[6] L. F. Mattheiss, E. M. Gyorgy, and D. W. Johnson, Superconductivity above 20 K in the Ba-K-Bi-O system, Phys. Rev. B **37**, 3745 (1988).

[7] M. Imada, A. Fujimori, and Y. Tokura, Metal-insulator transitions, Rev. Mod. Phys. **70**, 1039 (1998).

[8] D. Serrate, J. M. D. Teresa, and M. R. Ibarra, Double perovskites with ferromagnetism above room temperature, J. Phys.: Condens. Matter **19**, 023201 (2006).

[9] D. Xiao, W. Zhu, Y. Ran, N. Nagaosa, and S. Okamoto, Interface engineering of quantum Hall effects in digital transition metal oxide heterostructures, Nat. Commun. **2**, 596 (2011).

[10] J. He, A. Borisevich, S. V. Kalinin, S. J. Pennycook, and S. T. Pantelides, Control of Octahedral Tilts and Magnetic Properties of Perovskite Oxide Heterostructures by Substrate Symmetry, Phys. Rev. Lett. **105**, 227203 (2010).

[11] J. Chakhalian, J. M. Rondinelli, J. Liu, B. A. Gray, M. Kareev, E. J. Moon, N. Prasai, J. L. Cohn, M. Varela, I. C. Tung, M. J. Bedzyk, S. G. Altendorf, F. Strigari, B. Dabrowski, L. H. Tjeng, P. J. Ryan, and J. W. Freeland, Asymmetric orbital-lattice interactions in ultrathin correlated oxide films, Phys. Rev. Lett. **107**, 116805 (2011).

[12] S. Uchida, K. Kitazawa, and S. Tanaka, Superconductivity and metal-semiconductor transition in $BaPb_{1-x}Bi_xO_3$, Phase Transitions **8**, 95 (1987).

[13] N. C. Plumb, D. J. Gawryluk, Y. Wang, Z. Ristić, J. Park, B. Q. Lv, Z. Wang, C. E. Matt, N. Xu, T. Shang, K. Conder, J. Mesot, S. Johnston, M. Shi, and M. Radović, Momentum-resolved electronic structure of the high-T_c superconductor parent compound $BaBiO_3$, Phys. Rev. Lett. **117**, 037002 (2016).

[14] A. P. Menushenkov, A. V. Kuznetsov, K. V. Klementiev, and M. Y. Kagan, Fermi-bose mixture in $Ba(K)BiO_3$ superconducting oxide, J. Supercond. Nov. Magn. **29**, 701 (2016).

[15] A. E. Lukyanov, V. D. Neverov, Y. V. Zhumagulov, A. P. Menushenkov, A. V. Krasavin, and A. Vagov, Laser-induced ultrafast insulator-metal transition in $BaBiO_3$, Phys. Rev. Res. **2**, 043207 (2020).

[16] V. Meregalli and S. Y. Savrasov, Electron-phonon coupling and properties of doped $BaBiO_3$, Phys. Rev. B **57**, 14453 (1998).

[17] K. Foyevtsova, A. Khazraie, I. Elfimov, and G. A. Sawatzky, Hybridization effects and bond disproportionation in the bismuth perovskites, Phys. Rev. B **91**, 121114(R) (2015).

[18] G. Seibold and E. Sigmund, Metal-insulator transition in doped bismuthate superconductors, Solid State Commun. **86**, 517 (1993).

[19] R. Nourafkan, F. Marsiglio, and G. Kotliar, Model of the electron-phonon interaction and optical conductivity of $Ba_{1-x}K_xBiO_3$ superconductors, Phys. Rev. Lett. **109**, 017001 (2012).

[20] Y.-C. Yam, M. M. Moeller, G. A. Sawatzky, and M. Berciu, Peierls versus holstein models for describing electron-phonon coupling in perovskites, Phys. Rev. B **102**, 235145 (2020).

[21] G. Vielsack, W. Weber, P. Blaha, and K. Schwarz, Constraint-FLAPW calculations and determination of Hubbard model-parameters for $BaBiO_3$, in *Electronic Properties of High-Tc Superconductors*, edited by H. Kuzmany, M. Mehring, and J. Fink, Springer Series in Solid-State Sciences Vol. 113 (Springer, Berlin, Heidelberg, 1993), pp. 438–441.

[22] C. M. Varma, Missing valence states, diamagnetic insulators, and superconductors, Phys. Rev. Lett. **61**, 2713 (1988).

[23] Z. Li, G. Antonius, M. Wu, F. H. da Jornada, and S. G. Louie, Electron-phonon coupling from ab initio linear-response theory within the *GW* method: Correlation-enhanced interactions

and superconductivity in $Ba_{1-x}K_xBiO_3$, Phys. Rev. Lett. **122**, 186402 (2019).

[24] M. S. Hybertsen and S. G. Louie, Electron correlation in semiconductors and insulators: Band gaps and quasiparticle energies, Phys. Rev. B **34**, 5390 (1986).

[25] A. Khazraie, K. Foyevtsova, I. Elfimov, and G. A. Sawatzky, Oxygen holes and hybridization in the bismuthates, Phys. Rev. B **97**, 075103 (2018).

[26] F. Aryasetiawan, K. Karlsson, O. Jepsen, and U. Schönberger, Calculations of Hubbard U from first-principles, Phys. Rev. B **74**, 125106 (2006).

[27] L. Vaugier, H. Jiang, and S. Biermann, Hubbard U and Hund exchange J in transition metal oxides: Screening versus localization trends from constrained random phase approximation, Phys. Rev. B **86**, 165105 (2012).

[28] F. Nilsson, R. Sakuma, and F. Aryasetiawan, Ab initio calculations of the Hubbard U for the early lanthanides using the constrained random-phase approximation, Phys. Rev. B **88**, 125123 (2013).

[29] I. Timrov, N. Marzari, and M. Cococcioni, Hubbard parameters from density-functional perturbation theory, Phys. Rev. B **98**, 085127 (2018).

[30] B. Kim, K. Kim, and S. Kim, Quantification of Coulomb interactions in layered lithium and sodium battery cathode materials, Phys. Rev. Mater. **5**, 035404 (2021).

[31] N. Tancogne-Dejean and A. Rubio, Parameter-free hybridlike functional based on an extended Hubbard model: DFT+U+V, Phys. Rev. B **102**, 155117 (2020).

[32] M. Schüler, M. Rösner, T. O. Wehling, A. I. Lichtenstein, and M. I. Katsnelson, Optimal Hubbard models for materials with nonlocal Coulomb interactions: Graphene, silicene, and benzene, Phys. Rev. Lett. **111**, 036601 (2013).

[33] D. A. Prishchenko, V. G. Mazurenko, M. I. Katsnelson, and A. N. Rudenko, Coulomb interactions and screening effects in few-layer black phosphorus: a tight-binding consideration beyond the long-wavelength limit, 2D Mater. **4**, 025064 (2017).

[34] D. R. Penn, Wave-number-dependent dielectric function of semiconductors, Phys. Rev. **128**, 2093 (1962).

[35] Z. H. Levine and S. G. Louie, New model dielectric function and exchange-correlation potential for semiconductors and insulators, Phys. Rev. B **25**, 6310 (1982).

[36] M. S. Hybertsen and S. G. Louie, Model dielectric matrices for quasiparticle self-energy calculations, Phys. Rev. B **37**, 2733 (1988).

[37] G. Cappellini, R. Del Sole, L. Reining, and F. Bechstedt, Model dielectric function for semiconductors, Phys. Rev. B **47**, 9892 (1993).

[38] R. Petersen and T. G. Pedersen, Quasiparticle properties of graphene antidot lattices, Phys. Rev. B **80**, 113404 (2009).

[39] P. Cudazzo, I. V. Tokatly, and A. Rubio, Dielectric screening in two-dimensional insulators: Implications for excitonic and impurity states in graphane, Phys. Rev. B **84**, 085406 (2011).

[40] S. Latini, T. Olsen, and K. S. Thygesen, Excitons in van der Waals heterostructures: The important role of dielectric screening, Phys. Rev. B **92**, 245123 (2015).

[41] M. L. Trolle, T. G. Pedersen, and V. Véniard, Model dielectric function for 2D semiconductors including substrate screening, Sci. Rep. **7**, 39844 (2017).

[42] A. W. Sleight, Bismuthates: BaBiO$_3$ and related superconducting phases, Physica C Superconduc **514**, 152 (2015).

[43] T. M. Rice and L. Sneddon, Real-space and k$\rightarrow$-space electron pairing in BaPb$_{1-x}$Bi$_x$O$_3$, Phys. Rev. Lett. **47**, 689 (1981).

[44] A. Menushenkov, K. Klementev, P. Konarev, A. Meshkov, S. Benazeth, and J. Purans, The double-well oscillating potential of oxygen atoms in perovskite system Ba(K)BiO$_3$: EXAFS – analysis results, Nucl. Instrum. Methods Phys. Res., Sect. A **448**, 340 (2000).

[45] E. Berger, P. Valášek, and W. von der Linden, Two-dimensional Hubbard-Holstein model, Phys. Rev. B **52**, 4806 (1995).

[46] M. Tezuka, R. Arita, and H. Aoki, Phase diagram for the one-dimensional Hubbard-Holstein model: A density-matrix renormalization group study, Phys. Rev. B **76**, 155114 (2007).

[47] S. Johnston, E. A. Nowadnick, Y. F. Kung, B. Moritz, R. T. Scalettar, and T. P. Devereaux, Determinant quantum Monte Carlo study of the two-dimensional single-band Hubbard-Holstein model, Phys. Rev. B **87**, 235133 (2013).

[48] F. Becca, M. Tarquini, M. Grilli, and C. Di Castro, Charge-density waves and superconductivity as an alternative to phase separation in the infinite-U Hubbard-Holstein model, Phys. Rev. B **54**, 12443 (1996).

[49] R. P. Hardikar and R. T. Clay, Phase diagram of the one-dimensional Hubbard-Holstein model at half and quarter filling, Phys. Rev. B **75**, 245103 (2007).

[50] R. T. Clay and R. P. Hardikar, Intermediate phase of the one dimensional half-filled Hubbard-Holstein model, Phys. Rev. Lett. **95**, 096401 (2005).

[51] F. F. Assaad and T. C. Lang, Diagrammatic determinantal quantum Monte Carlo methods: Projective schemes and applications to the Hubbard-Holstein model, Phys. Rev. B **76**, 035116 (2007).

[52] A. Macridin, G. A. Sawatzky, and M. Jarrell, Two-dimensional Hubbard-Holstein bipolaron, Phys. Rev. B **69**, 245111 (2004).

[53] M. Capone, G. Sangiovanni, C. Castellani, C. Di Castro, and M. Grilli, Phase separation close to the density-driven Mott transition in the Hubbard-Holstein model, Phys. Rev. Lett. **92**, 106401 (2004).

[54] E. A. Nowadnick, S. Johnston, B. Moritz, R. T. Scalettar, and T. P. Devereaux, Competition between antiferromagnetic and charge-density-wave order in the half-filled Hubbard-Holstein model, Phys. Rev. Lett. **109**, 246404 (2012).

[55] Y. Murakami, P. Werner, N. Tsuji, and H. Aoki, Ordered phases in the holstein-hubbard model: Interplay of strong Coulomb interaction and electron-phonon coupling, Phys. Rev. B **88**, 125126 (2013).

[56] P. Werner and A. J. Millis, Efficient Dynamical Mean Field Simulation of the Holstein-Hubbard Model, Phys. Rev. Lett. **99**, 146404 (2007).

[57] N. C. Costa, K. Seki, S. Yunoki, and S. Sorella, Phase diagram of the two-dimensional Hubbard-Holstein model, Commun. Phys. **3**, 80 (2020).

[58] S. Sugai, S. Uchida, K. Kitazawa, S. Tanaka, and A. Katsui, Lattice vibrations in the strong electron-phonon-interaction system BaPb$_{1-x}$Bi$_x$O$_3$ studied by raman scattering, Phys. Rev. Lett. **55**, 426 (1985).

[59] S. Tajima, M. Yoshida, N. Koshizuka, H. Sato, and S. Uchida, Raman-scattering study of the metal-insulator transition in Ba$_{1-x}$K$_x$BiO$_3$, Phys. Rev. B **46**, 1232 (1992).

[60] T. O. Wehling, E. Şaşıoğlu, C. Friedrich, A. I. Lichtenstein, M. I. Katsnelson, and S. Blügel, Strength of effective Coulomb interactions in graphene and graphite, Phys. Rev. Lett. **106**, 236805 (2011).

[61] P. Giannozzi, S. Baroni, N. Bonini, M. Calandra, R. Car, C. Cavazzoni, D. Ceresoli, G. L. Chiarotti, M. Cococcioni, I. Dabo, A. D. Corso, S. de Gironcoli, S. Fabris, G. Fratesi, R. Gebauer, U. Gerstmann, C. Gougoussis, A. Kokalj, M. Lazzeri, L. Martin-Samos *et al.*, QUANTUM ESPRESSO: a modular and open-source software project for quantum simulations of materials, J. Phys.: Condens. Matter **21**, 395502 (2009).

[62] G. Pizzi, V. Vitale, R. Arita, S. Blügel, F. Freimuth, G. Géranton, M. Gibertini, D. Gresch, C. Johnson, T. Koretsune, J. Ibañez-Azpiroz, H. Lee, J.-M. Lihm, D. Marchand, A. Marrazzo, Y. Mokrousov, J. I. Mustafa, Y. Nohara, Y. Nomura, L. Paulatto *et al.*, Wannier90 as a community code: new features and applications, J. Phys.: Condens. Matter **32**, 165902 (2020).

[63] http://www.pseudo-dojo.org/.

[64] N. Marzari, A. A. Mostofi, J. R. Yates, I. Souza, and D. Vanderbilt, Maximally localized wannier functions: Theory and applications, Rev. Mod. Phys. **84**, 1419 (2012).

[65] F. Giustino, Electron-phonon interactions from first principles, Rev. Mod. Phys. **89**, 015003 (2017).